The Origin of a Preeruptive Magnetic Structure with Significant Nonneutralized Electric Current

Wensi Wang[1,2] , Rui Liu[1,2] , Jiong Qiu[3] , Jinhan Guo[4,5] , and Yuming Wang[1,6]

[1] CAS Key Laboratory of Geospace Environment, Department of Geophysics and Planetary Sciences, University of Science and Technology of China, Hefei 230026, People's Republic of China; minesnow@ustc.edu.cn
[2] Mengcheng National Geophysical Observatory, University of Science and Technology of China, Hefei 230026, People's Republic of China
[3] Department of Physic, Montana State University, Bozeman, MT 59717, USA
[4] School of Astronomy and Space Science and Key Laboratory for Modern Astronomy and Astrophysics, Nanjing University, Nanjing 210023, People's Republic of China
[5] Centre for Mathematical Plasma Astrophysics, Department of Mathematics, KU Leuven, Celestijnenlaan 200B, B-3001 Leuven, Belgium
[6] National Key Laboratory of Deep Space Exploration, Deep Space Exploration Laboratory/School of Earth and Space Sciences, University of Science and Technology of China, Hefei 230026, People's Republic of China

Abstract

The buildup of the preeruptive magnetic field configuration and the eruption onset mechanism are critical yet poorly understood in solar eruptions. Coronal structures like sigmoids and filaments have been identified as preeruptive magnetic structures; their associated preflare motions as well as preflare brightenings have been identified as precursor signatures, yet none of these definitively lead to eruptions, and the cause and effect is contentious. Most importantly, how the preeruptive coronal structure evolves with the photospheric magnetic field is elusive. Here we report the development of the photospheric nonneutralized electric current associated with the buildup of a preeruptive coronal structure observed as a bundle of hot low-lying coronal loops collectively taking a sigmoidal shape. The significant nonneutralized electric current appeared several hours ahead of the formation of the preeruptive structure. The buildup of the preeruptive structure in the corona was simultaneous with the gradual extension of the nonneutralized electric current in the photosphere. The synchronous evolution seemed to stop when intermittent brightening occurred along the preeruptive structure in the corona. The preflare brightening lasted for about 4 hr, with two ribbon-like structures matching the nonneutralized electric current. Eventually, the preeruptive structure evolved into a magnetic flux rope (MFR) and erupted. Quantitative measurements indicate that the significant nonneutralized electric current also flows through the footpoints of the erupting MFR, which are well identified by a pair of conjugate dimmings. The evolution of the photospheric nonneutralized electric current is demonstrated to signal the buildup of the preeruptive structure and the imminent eruption.

Unified Astronomy Thesaurus concepts: Solar flares (1496); Solar coronal mass ejections (310); Solar magnetic fields (1503)

Materials only available in the online version of record: animations

1. Introduction

Large-scale solar eruptions, especially coronal mass ejections (CMEs), are the strongest driver of adverse space weather close to the Earth. These phenomena are believed to be powered by so-called free magnetic energy in the current-carrying magnetic fields, such as a magnetic flux rope (MFR), a sheared magnetic arcade (SMA), or even an SMA–MFR hybrid structure (a more detailed definition can be found in a review paper; S. Patsourakos et al. 2020). Now a broad consensus is that most CMEs will contain an MFR after the eruption. But the nature of the preeruptive magnetic configuration of CMEs is still under debate. The more important question will be how the preeruptive magnetic configuration forms in the Sun and further evolves toward eruptions.

Previous three-dimensional (3D) simulations predict that a subphotospheric twisted flux tube will partially emerge into the corona, either directly forming as a coherent MFR during the emergence process or further generating a new MFR via magnetic reconnection (Y. Fan 2001; T. Magara & D. W. Longcope 2003; V. Archontis et al. 2004; Y. Fan & S. E. Gibson 2004; V. Archontis & T. Török 2008; V. Archontis & A. W. Hood 2010, 2012). The latter is related to the tether-cutting reconnection (R. L. Moore & G. Roumeliotis 1992) or the flux cancellation reconnection (A. A. van Ballegooijen & P. C. H. Martens 1989), when the part of the emerging flux tube manifests as an arcade. Meanwhile, the timing of the MFR formation is a crucial issue to decide possible mechanisms for solar eruptions. Nowadays, it is well accepted that the eruption of preexisting MFRs will be triggered by an ideal MHD instability, such as torus instability (B. Kliem & T. Török 2006) and kink instability (A. W. Hood & E. R. Priest 1979; T. Török & B. Kliem 2005), and subsequently driven by magnetic reconnection. A recent simulation from Q. Liu et al. (2024) demonstrates that magnetic reconnection can primarily trigger and drive the eruption of a preexisting MFR. Additionally, the magnetic reconnection will be the trigger of the eruption in the absence of the MFR, i.e., tether-cutting reconnection (R. L. Moore et al. 2001) and magnetic breakout reconnection (S. K. Antiochos et al. 1999).

The observational proxies of the preeruptive magnetic configuration, such as filaments/prominences, sigmoids, cavities, and hot channels, have been extensively investigated in

previous studies. The majority of studies suggest that sigmoids (D. M. Rust & A. Kumar 1996; L. M. Green et al. 2007, 2011; R. Liu et al. 2010; A. S. Savcheva et al. 2014), cavities (S. E. Gibson & Y. Fan 2006; S. E. Gibson et al. 2010), and hot channels (J. Zhang et al. 2012; X. Cheng et al. 2013) should be the manifestation of the MFR topology. But both an MFR and an SMA can be good candidates for filaments/prominences. However, in the absence of direct measurement of the coronal magnetic fields, it poses a major challenge to determine the preeruptive magnetic configuration from observations. Aided by the nonlinear force-free field (NLFFF) modeling, the preeruptive configuration can be identified through mapping magnetic connectivities and computing the twist number (R. Liu et al. 2016), such as a double-decker flux rope system (R. Liu et al. 2012; B. Kliem et al. 2014) and a multi-flux-rope system (A. K. Awasthi et al. 2018). Another alternative approach is to investigate the erupting magnetic structures' feet from observations (D. F. Webb et al. 2000; J. Qiu et al. 2007; W. Wang et al. 2017, 2019; C. Xing et al. 2020). The evolution of preeruptive magnetic structures could be effectively monitored by tracking the temporal evolution of its footpoints, which can be well identified by conjugate coronal dimmings and bright hooks (M. Janvier et al. 2014; J. Qiu & J. Cheng 2017; W. Wang et al. 2019; K. Barczynski et al. 2020; T. Gou et al. 2023).

Recently, W. Wang et al. (2023, hereafter Paper I) conducted a statistical study to investigate the preeruptive magnetic properties of 28 erupting MFRs. All footpoints of the MFRs were identified by conjugate coronal dimmings. The results indicated two MFR categories, one carrying significant nonneutralized current and the other carrying neutralized current. For an isolated flux tube model, the main (direct) current is surrounded by the shielding (return) current in equal amounts and opposite directions, resulting in neutralized current (D. B. Melrose 1991; E. N. Parker 1996). In Paper I, the degree of current neutralization R_z (the magnitude ratio of direct current, DC, over return current, RC) measured at the footpoints of the erupting MFR is used to assess whether the MFR is current neutral. We found eight MFRs with significant nonneutralized current ($R_z > 2.0$; more detailed calculations can be found in Section 2 of Paper I). R. Liu & W. Wang (2024) found nine additional eruptive events that conform to the criteria in Paper I for MFR eruptions and subsequently examined the footpoints of these nine MFRs using the same method as described in Paper I. Only two out of the nine MFRs contain significant nonneutralized current. Therefore, we have already found 10 MFRs carrying significant nonneutralized current. These MFRs remind us of previous numerical experiments that nonneutralized current will be injected into the active regions during the emergence of the twisted flux rope with neutralized current into the corona (K. D. Leka et al. 1996; D. W. Longcope & B. T. Welsch 2000; J. E. Leake et al. 2013; T. Török et al. 2014). Previous observational studies further indicate that the nonneutralized electric current in the solar active regions will be a better proxy for assessing the CME productivity (M. K. Georgoulis et al. 2012; Y. Liu et al. 2017; I. Kontogiannis et al. 2019; E. A. Avallone & X. Sun 2020). Y. Liu et al. (2024) recently conducted a representative sample of 18 eruptive flares and 10 confined flares to investigate the relationship between the degree of current neutralization and the CME productivity of the active regions. Their result further confirms that |DC/RC| is a good proxy for assessing CME productivity. A. Duan et al. (2024) did a systematic survey of |

DC/RC| in a larger sample of 86 emerging active regions and found that the correlation between |DC/RC| and nonpotentiality of the fields is high. I. Kontogiannis & M. K. Georgoulis (2024) have examined the temporal evolution of nonneutralized current in 59 emerging active regions and revealed that the complexity of active regions hinders the use of simple parameters for eruption prediction.

Therefore, investigating the formation and evolution of these MFRs carrying significant nonneutralized current can provide valuable insights into the underlying mechanisms of solar eruptions. Here we study one representative example of the MFR with significant nonneutralized electric current from Paper I and aim to figure out how these MFRs form and erupt in the Sun. The overview of the studied event is in Section 2. Impressively, we found the synchronous buildup of elongated nonneutralized current and the preeruptive coronal structure 10 hr prior to the eruption (see Section 3). We further tracked the formation of elongated DC until the appearance of the MFR in the corona (see Section 4). Then preflare ribbons were found along the MFR 5 hr ahead of the onset of the flare (see Section 5). We also employed data-driven MHD simulation (J. H. Guo et al. 2024) to discuss the formation and eruption of the MFR with nonneutralized current (see Section 6).

2. Data and Methodology

2.1. Overview of the August 2 Event

The eruption of interest occurred in the active region NOAA 11261 on 2011 August 2. It produced an M1.4-class long-duration flare observed by the Solar Dynamics Observatory (SDO; W. D. Pesnell et al. 2012) and the Solar TErrestrial RElations Observatory (STEREO; M. L. Kaiser et al. 2008). The Atmospheric Imaging Assembly (AIA; J. R. Lemen et al. 2012) on board the SDO provides seven EUV passbands and two UV passbands. In this study, we mainly used the 94 Å, 304 Å, and 1600 Å channels to investigate the coronal structure, coronal dimmings, and preflare/flare ribbons. Figure 1 shows snapshots of the studied eruption from SDO observations. From SDO's perspective, the eruption occurred near the center of the solar disk; see Figures 1(b1)–(b3). A obvious flux-rope-like structure was observed prior to the onset of the flare (see Figure 1(b1)), which finally evolved into a halo CME captured by the COR2 coronagraph on board STEREO. During the eruption, a pair of coronal dimmings was found on two sides of the flare ribbons and associated with opposite magnetic polarities when projected into the magnetogram (see Figures 1(b3) and (c)), labeled as "conjugate dimmings." The appearance of dimmings was only several minutes ahead of the onset of the flare, which is termed the posteruption dimming. The two contours in Figure 1 cover all the dimmed pixels, which are considered the core feet of the erupting MFR. The detailed information about the detection of dimmings and identification of the MFR's footpoints can be found in Paper I.

2.2. Measuring Temperature Information and Magnetic Properties of the MFR

Here we use the differential emission measure (DEM) diagnostics to obtain the temperature information of the MFR based on six AIA EUV channels. We apply the modified DEM code (M. C. M. Cheung et al. 2015; Y. Su et al. 2018) to calculate emission measures (EMs) by integrating DEM over the temperature range of $\log T = 5.5$–7.6 with a interval of
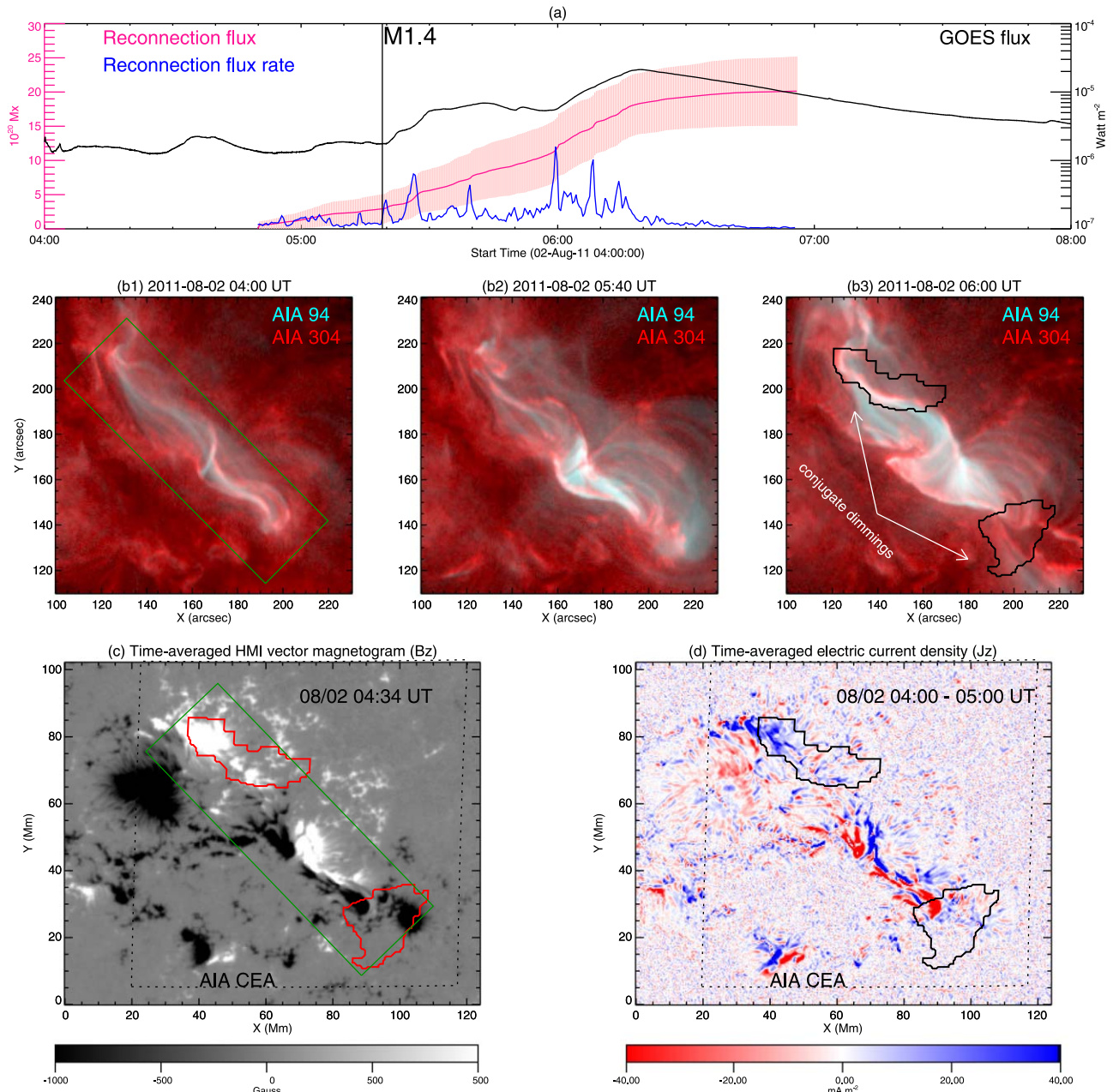
Figure 1. Overview of the 2011 August 2 event. (a) The soft X-ray light curve (black) from GOES of the long-duration M1.4-class flare, the magnetic reconnection flux (pink; shadow for errors), and the time derivatives of the magnetic reconnection flux (blue). (b) The superimposed images from the AIA 94 Å and 304 Å passbands, showing the preeruptive structure (b1), the erupting MFR (b2), and the pair of conjugate dimmings (b3). (c) The preeruptive magnetic field from the Helioseismic and Magnetic Imager (HMI). (d) The map of vertical electric current density, which is averaged over 1 hr. The two contours in the panels are the identified footpoints of the MFR. An animation of the superimposed images from AIA 94 Å and 304 Å is available. The animation proceeds from 19:20 UT on 2011 August 1 to 07:00 UT on 2011 August 2, encompassing the complete evolution of the MFR. (An animation of this figure is available in the online article.)

$\Delta \log T = 0.05$. In this study, we used the EM-weighted mean temperature to provide the temperature distribution of the MFR. The EM-weighted mean temperature was generated by deriving $\overline{T}$ over the entire temperature range based on the following equation:

$$\overline{T} = \frac{\sum \mathrm{EM}(T_i) \times T_i}{\sum \mathrm{EM}(T_i)}.$$

Here we use the Space weather HMI Active Region Patch (SHARP) data, which are disambiguated and deprojected to the heliographic coordinates with a Lambert (cylindrical equal area) projection method (M. G. Bobra et al. 2014). Then the vertical electric current density (j_z) can be estimated using Ampère's law $\mathbf{j} = \frac{1}{\mu_0}(\nabla \times \mathbf{B})$ based on the Helioseismic and Magnetic Imager (HMI) vector magnetogram. The results from Paper I show that most low signal-to-noise pixels can be well eliminated by averaging j_z over several hours. A longer averaging time will more effectively reduce noise; however, it may also diminish the dynamic characteristics of the electric current. In this study, we prefer 1 hr average maps to better

exhibit the dynamic evolution of the electric current. More detailed comparison between the original electric currents and the time-averaging currents can be found in Paper I. By projecting two conjugate dimming regions onto the HMI vector magnetogram, we can estimate the magnetic fluxes and vertical electric current of the erupting MFR. The order of magnitude of the magnetic fluxes and the DC in two footpoints are about 10^{21} Mx and 10^{12} A.

In this study, we followed the definition of current neutralization from Y. Liu et al. (2017) and utilized the degree of current neutralization ($R_z = |I_{DC}/I_{RC}|$) to determine the nonneutralized current. For the positive (negative) magnetic field, I_{DC} is computed by integrating j_z with the dominant sign of j_z/B_z in that field, whereas I_{RC} is computed by integrating j_z with the opposite sign. The magnetic field is considered to be carrying significant nonneutralized current when the value of R_z exceeds 2.0. The degree of current neutralization of the footpoint related to the positive field is about 3.6, suggesting that the MFR possesses significant nonneutralized current. It is noteworthy that the identified footpoints are anchored at the far ends of two smoothing electric current ribbons (Figure 1(d)).

2.3. Helicity and Energy Input of the Host Active Region

To monitor the dynamic evolution of the host active region, we calculated transverse photospheric velocity by applying the Differential Affine Velocity Estimator for Vector Magnetograms (DAVE4VM; P. W. Schuck 2008) to time-series HMI vector magnetograms. Then we can estimate the relative helicity injection rate and the Poynting flux across the photospheric boundary S of the host active region by the following formulae (R. Liu et al. 2016):

$$\frac{dH}{dt}\Big|_s = 2 \int_S (\boldsymbol{A_p} \cdot \boldsymbol{B_t}) V_{\perp n} \; dS - 2 \int_S (\boldsymbol{A_p} \cdot \boldsymbol{V_{\perp t}}) B_n \; dS,$$

$$\frac{dP}{dt}\Big|_s = \frac{1}{4\pi} \int_S B_t^2 V_{\perp n} \; dS - \frac{1}{4\pi} \int_S (\boldsymbol{B_t} \cdot \boldsymbol{V_{\perp t}}) B_n \, dS,$$

where B_p is the reference potential field and A_p is the vector potential of B_p; the subscripts t and n refer to the tangential and normal directions, respectively.

In this study, we present 1 hr average j_z maps to more effectively illustrate the dynamic evolution of the electric current. The 3 hr average velocity maps are utilized to better highlight the shear flows. Nonetheless, all physical quantities, including magnetic flux, electric current, helicity flux, Poynting flux, and more, were calculated based on the original SHARP data.

3. Synchronous Evolution of a Preeruptive Magnetic Structure and the Photospheric Field

A bright, slightly twisted coherent structure was first observed in the AIA 94 Å passband at about 19:30 UT, marked as T0 in the following figures, almost 10 hr prior to the initiation of the M1.4-class flare (see the corresponding animation of Figure 1). This coronal structure was invisible in AIA's cool passbands, e.g., 171, 193, 211, and 304 Å. The DEM diagnostic confirms that the bright coherent structure is a hot structure whose temperature ranges from 5 to 15 MK during the entire evolution. More impressively, a strong electric current ($j_z > 40$ mA m^{-2}) is concentrated around the bright twisted structure.

To make a more comprehensive comparison between the evolution of the strong electric current and the coronal structure, we zoom into the region covering both features (the rectangle in Figures 1(b1) and (c)) and reorient the rectangles in the direction of motion (Figure 2). We then outline the bright coronal structure in the AIA 94 Å passband (black symbols in Figure 2(a1)) and reproject into the HMI vector magnetogram (green cross symbols in Figure 2(b1)). One footpoint of this coronal structure was anchored at a positive field that was dominated by the strong positive current, labeled as "FP+" (the square in Figure 2). The other footpoint was cospatial with the negative field that was dominated by the strong negative current, labeled as "FP−" (the short transverse line in Figure 2). In the following 5 hr, the FP− was moving with the slow extension of the negative electric current. No obvious change in the shape of this structure was found at this period even after the occurrence of two small C-class flares. At about 23:00 UT, two groups of bright loops were visible near the bright coronal structure. Subsequently, continuous brightening was observed in the vicinity of the FP−, implying the occurrence of magnetic reconnection in the corona. Then the length and thickness of the bright twisted structure quickly increased, manifested as more and more twisted loops wrapping into it. Meanwhile, starting from about August 2 00:30 UT, the synchronous evolution between the bright coronal structure and photospheric nonneutralized currents seems to be disrupted. The FP− was moving faster and slipping along the negative current, finally stopping at the end of the elongated current when a highly twisted flux-rope-like structure was observed in the corona (Figure 2(a8)). At about 04:00 UT, the highly twisted flux rope started to rise and then rapidly erupted (Figures 1(b1)–(b3)).

The temperature of this coherent structure exhibited a continuous increase several hours prior to the eruption. The temperature distribution of the structure is shown in Figure 3. The initial appearance of the coherent structure in the corona exhibited a uniform temperature distribution, with an approximate value of 4–5 MK. In the following 5 hr, the synchronous evolution stage, its temperature fluctuated between 5 and 7 MK. The core of the coronal structure was heating up to around 10 MK at August 2 01:40 UT (T1; the vertical dashed line in Figure 3). Then its temperature still remained around 5–6 MK until the onset of eruption. To quantify the temperature evolution of the twisted structure, we plot temperature variation curves for the coronal structure and the FP+ calculating from identified points in the AIA 94 Å passband (Figure 3(c)). The mean temperature of the coronal structure exhibited a similar enhancement, ranging from 4 to 6 MK. For the coronal structure (the red curve in Figure 3(c)), the temperature reached the maximum value during the C-class flare. But for the FP+ (the black curve in Figure 3), the maximum occurred at around August 2 04:30 UT. Significant distinctions could be observed in AIA passbands. Figures 3(a) and (b) show the average brightness of the coronal structure and the FP+ during the preeruptive phase, respectively. The maximum brightness of the coronal structure occurred during the C-class flares (the arrows in Figure 3). However, for the FP+, the maximum occurred around August 2 01:40 UT. The period between August 1 23:30 UT and August 2 01:40 UT will be the most important evolutionary stage for the buildup of the highly twisted flux rope.

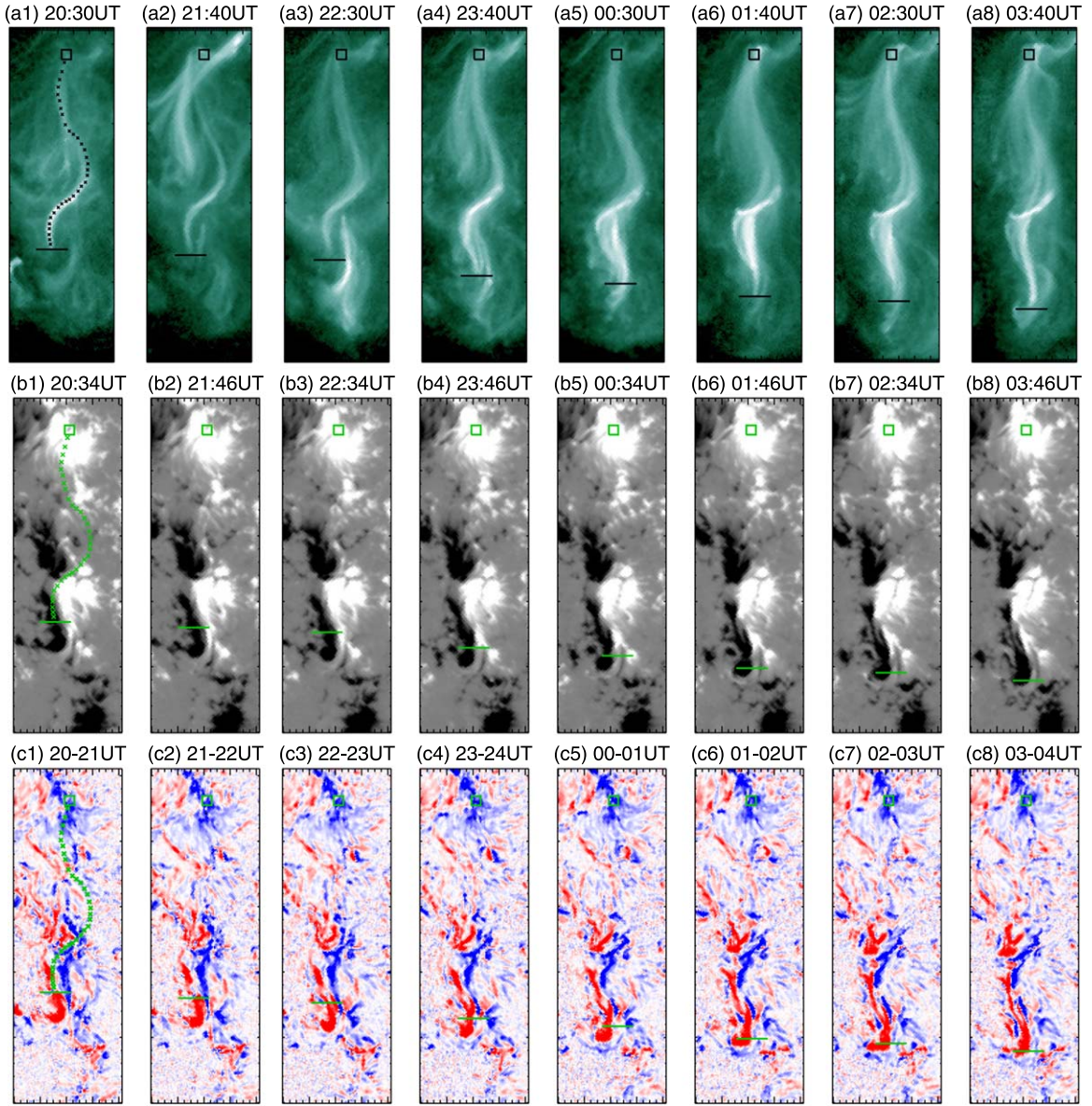The evolution of the photospheric field can be found in Figure 4 and the corresponding animation. In order to

Wang et al.

Figure 2. The synchronous evolution of the coronal coherent structure and the photospheric field. (a) The evolution of the preeruptive coherent structure in AIA 94 Å. (b) The evolution of the B_z. (c) The dynamic evolution of significant nonneutralized current for the negative field. The cut images from AIA 94 Å and HMI sharp data are aligned. The boxes mark the fixed footpoint of the coronal coherent structure, and the short transverse lines mark the moving footpoint. The magnetic field and current density maps are scaled the same as in Figure 1.

quantitatively compare the evolution of the photospheric field and the coronal structure, we estimated the magnetic fluxes (Φ), vertical electric currents (I), averaged transverse field (B_h), and relative helicity flux injection rate (dH/dt) within the black rectangle in Figure 4(a) from August 1 08:00 UT to August 2 07:00 UT. The temporal evolution of the positive field and negative field parameters were illustrated in Figures 4(e) and (f), respectively. For the positive field, the positive flux Φ_+ (black curve), the mean horizontal component of the magnetic field $|B_h|$ (green curve), and the positive current I_+ (blue curve) were all exhibiting similar bimodal distributions (Figure 4(e)). The first peak of these parameters occurred several minutes prior to the appearance of the bright coherent structure in AIA 94 (August 1 19:30 UT, labeled as T0), while the second peak of them just occurred around the heating time of the bright coherent structure (August 2 01:40 UT, labeled as T1). Similar bimodal distributions were also found in the negative field

(Figure 4(f)). The $|B_h|$ (green curve) and the negative current I_- (blue curve) reached the first peak several minutes ahead of the T0 and then reached the second peak around the T1. Different from the Φ_+, the negative flux Φ_- continued to increase during the whole period, manifested as two-stage rapid enhancement. But the first rapid rise of Φ_- stopped at T0, and its second rise stopped at T1. The rapid injection of the positive helicity flux dH/dt (red curve in Figures 4(e) and (f)) occurred ahead of the T0. The unchanged and slight decrease of dH/dt occurred during the synchronous evolution of coronal coherent structure and the nonneutralized currents. Then the dH/dt quickly decreased after the T1.

The bimodal temporal evolution of the photospheric field is highly matched with the two-stage evolution of the bright coronal structure. The appearance of the bright coronal structure lagged behind the first peak of the magnetic fluxes (Φ_+ and Φ_-), the mean horizontal component of the magnetic field ($|B_h|$), and the
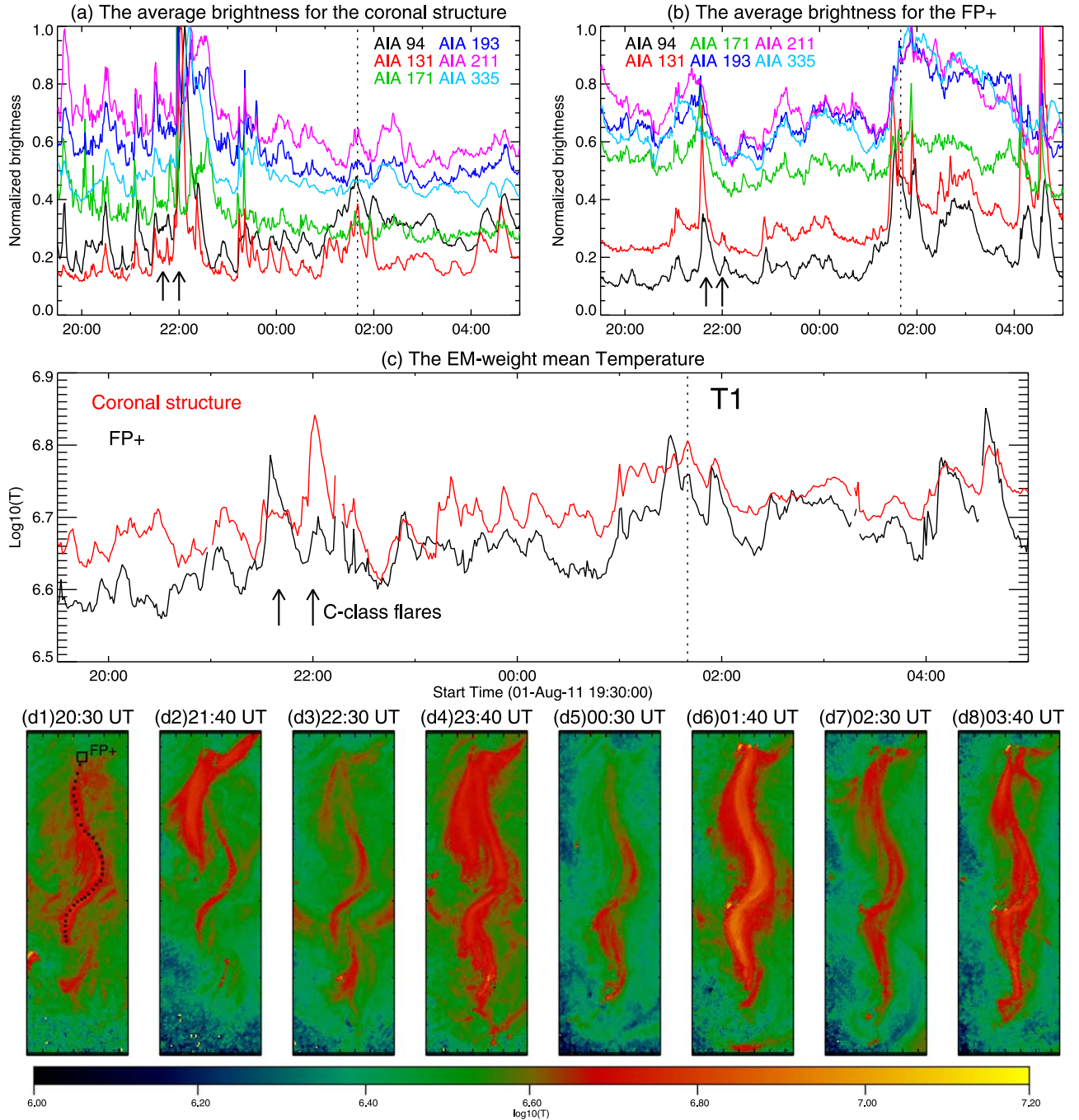
Figure 3. The temperature evolution of the coronal coherent structure. The panels in the bottom show the distribution of the EM-weight temperature of the coronal structure from August 1 20:30 UT to August 2 03:40 UT. (a) The evolution of the normalized brightness of the coronal structure in AIA passbands. (b) The evolution of the normalized brightness of the FP+ region in AIA passbands. (c) The evolution of the average temperature of the coronal structure (the red curve) and the FP+ region (the black curve). The black points in (d1) outline the coronal structure and are utilized to calculate its average brightness and temperature. The small box in (d1) marks the FP+ region of the coronal structure.

electric currents (I_+ and I_-) by several minutes. In the subsequent 4 hr, the magnetic fluxes (Φ_+ and Φ_-) and electric currents (I_+ and (I_-)) dropped to the flat regions simultaneously. The B_h of the positive and negative fields exhibited a rapid decrease, followed by a gradual increase during this period. At about 23:30 UT, the dH/dt of the negative field reached the maximum value. Meanwhile, the heating occurred around the moving FP (FP−). Then the temperature of the coronal structure reached its maximum value at August 2 01:40 UT; meanwhile, the magnetic fluxes, the mean transverse field, and the electric currents also rose to the second peak. Then these magnetic parameters

subsequently exhibited a gradual decrease except for the Φ_-. These observations indicate that photospheric evolution should play a direct role in driving the buildup of the coronal coherent structure.

4. Formation and Evolution of Nonneutralized Electric Current in the Photosphere

The significant nonneutralized current in this event also manifested as elongated structure bracketing the polarity inversion line (PIL) segment, resembling the elongated DCs
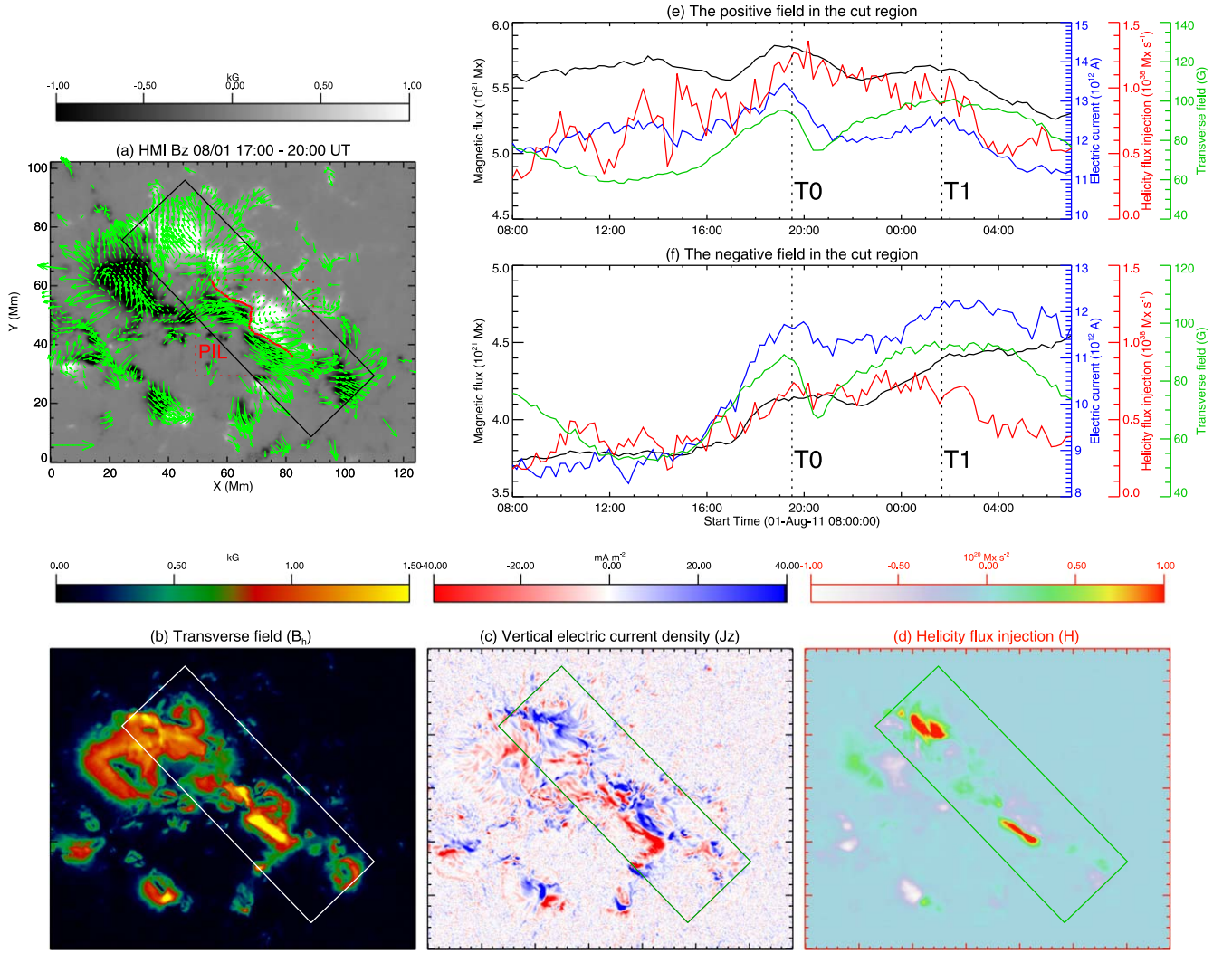
Figure 4. The evolution of the photospheric field. (a)–(d) represent the 3 hr averaged parameters of the photospheric field: transverse velocity (green arrows), transverse field (B_h), vertical electric current density, and relative helicity flux injection rate. (e) and (f) show the temporal evolution of these parameters in the cut region calculated from the positive field (e) and negative field (f), including the magnetic fluxes (black curve), electric current (blue curve), average transverse field (green curve), and helicity flux injection (red). The rectangles of different colors in all snapshots delineate the cut region, while the dashed red box in (a) outlines the location of the PIL. Two dashed lines (T0 and T1) mark two important moments of the coronal coherent structure, the moment of appearance (T0) and the maximum temperature (T1). An animation of the velocity field, transverse field, vertical electric current density, and relative helicity flux injection rate are available. The animation proceeds from 08:00 UT on 2011 August 1 to 07:00 UT on 2011 August 2, showing the evolution of the photospheric field.

(An animation of this figure is available in the online article.)

consistently observed during eruptive X-class flares (Y. Liu et al. 2024). Before August 1 12:00 UT, positive and negative electric currents randomly distributed along the PIL region (see the Figure 4 animation and Figure 5(c1)). Then they gradually separated and converged toward the regions with the same polarity of the magnetic field. Then the negative field was gradually occupied by the negative current, leading to an increase in the degree of current neutralization R_z (the red curve in Figure 5(a)), calculated within the negative field in this box. The R_z reached its maximum value of 2.2 at about 16:00 UT, subsequently exhibiting minor fluctuations within the range of 2.0–2.2, suggesting that the nonneutralized current formed in the negative field. The nonneutralized current began to extend outward along the PIL region at 16:00 UT (see the Figure 4 animation). In the following hours, the elongated nonneutralized current appeared along the PIL region (see Figure 5(c4)).

Strong shearing flows were observed along the PIL region during the formation of the elongated nonneutralized

current (Figure 5(b4)). To quantify the shearing flows, we calculated the velocity shear angle θ, which represents the angular deviation between the PIL region and the velocity vector. The PIL segment that is aligned with the elongated nonneutralized current was used to calculate the θ. The black curve in Figure 5(a) illustrates the temporal variation of the mean θ value along the PIL segment. Initially, the velocities were perpendicular to the PIL segment, and then they were gradually turned parallel to the PIL segment, resulting in the slow decrease of θ. The θ was dropping at a rate of $4.\!^{\circ}65$ hr^{-1} linearly. Eventually, the θ reached to the minimum value of 25° around 19:30 UT, forming strong shearing flows. These shearing flows predominantly occurred within the negative magnetic field at speeds ranging from 1 to 2 km s^{-1}. At around 16:00 UT, θ decreased to half of the initial value (about 40°). The horizontal component of the photospheric magnetic field B_h was enhanced primarily on the regions encompassing the elongated nonneutralized current
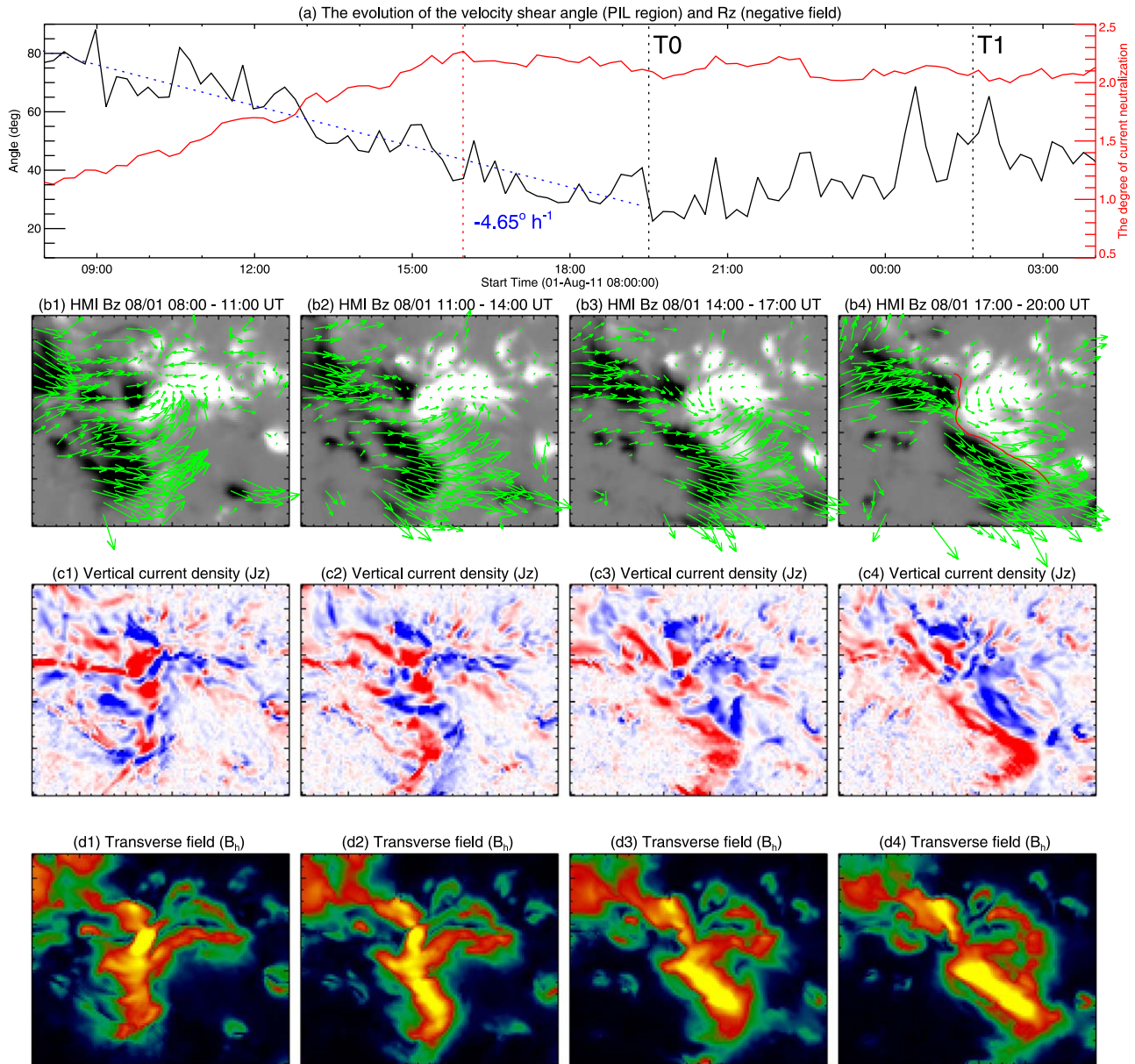
Figure 5. Formation of the significant nonneutralized current. (a) The evolution of the velocity shear (black curve) angle along the PIL region (red curve in (b4)) and the degree of current neutralization R_z calculated from the negative field in the region ((b) and the red box in Figure 4(a)). (b) The evolution of the velocity before the formation of the nonneutralized current. (c) The formation of the nonneutralized current. (d) The evolution of the transverse field. The snapshots are cut from the PIL region (the red dashed box) in Figure 4(a).

(Figures 5(d3) and (d4)), showing a strip-like structure with a similar extension as the elongated nonneutralized current since 16:00 UT (see the Figure 4 animation). In contrast, positive helicity fluxes are mainly injected at the two footpoints of the coronal structure (Figure 4(d)).

5. The Preflare Reconnection

The coronal coherent structure has experienced multiple episodes of heating since August 1 23:00 UT (Figure 3(c)). These heating process are most likely related to magnetic reconnection that occurred prior to the eruption. Preflare bright ribbons were observed in the AIA 304 Å passband 5 hr before the onset of the M-class flare. Figure 6 and the corresponding animation show the preflare ribbons along the coronal coherent structure. In contrast to the observations of bright coronal structure in the AIA 94 Å passband, a channel-

like structure appeared in the AIA 304 Å passband (Figure 6(b1)). Two footpoints of the bright coherent structure in the AIA 94 Å passband were cospatial with two ends of the channel-like structure in AIA 304 Å, indicating that two structures are inherently associated with the same magnetic configuration. The bright points surrounding the channel evolved into two bright ribbons (labeled as "PR+/−" in Figure 6(b3)), which eventually transformed into the typical flare ribbons (marked as "R+/−" in Figure 6(c4)) during the eruption, implying their association with magnetic reconnection.

All bright pixels underneath the coronal coherent structure were detected in the AIA 304 Å passband and reprojected into the HMI vector magnetogram to calculate the preflare ribbon flux (the red curve in Figure 6(a)). The preflare ribbon flux is highly correlated with the GOES soft X-ray
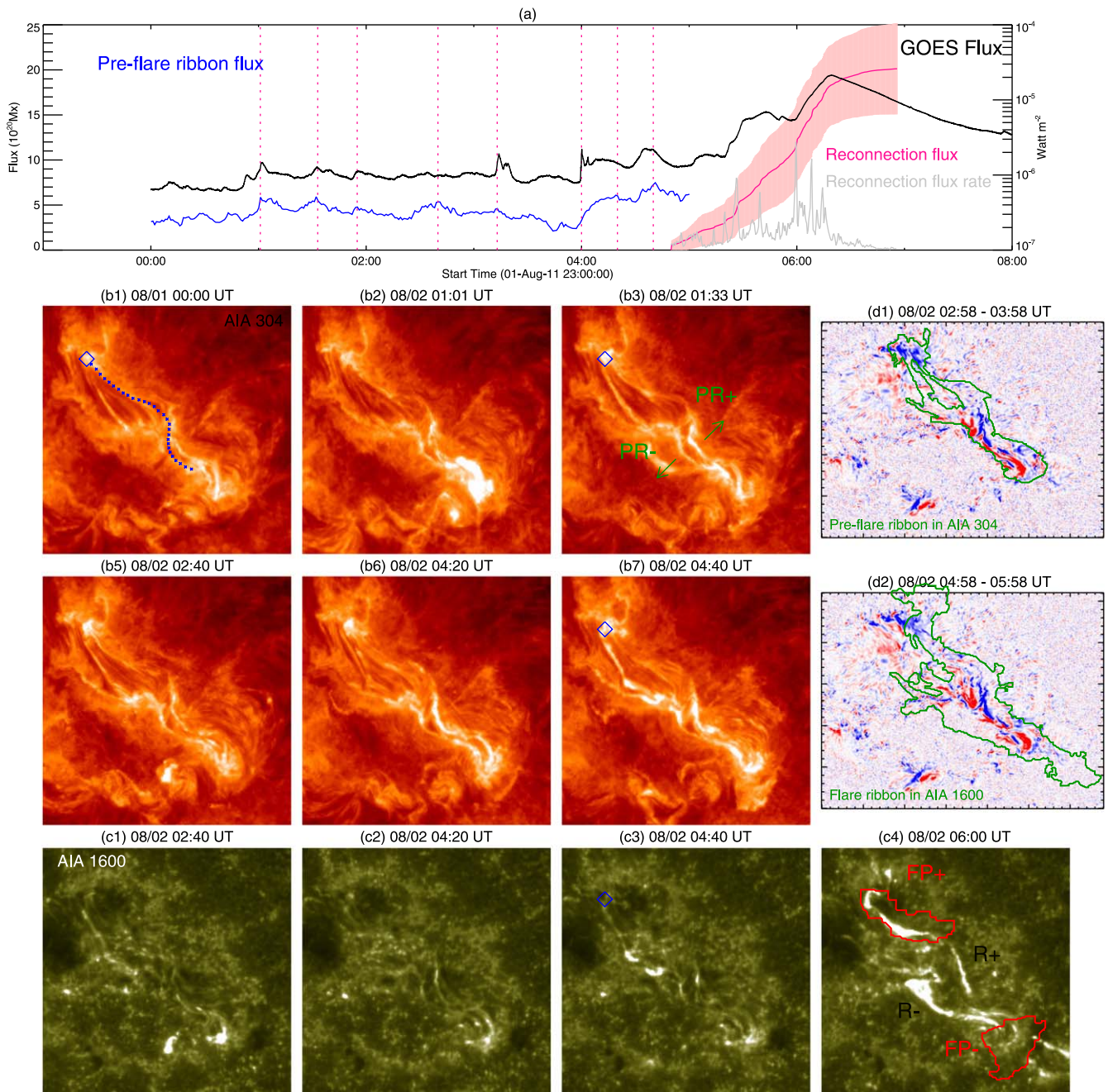
Figure 6. The preflare ribbons. (a) The temporal evolution of the preflare ribbon flux calculated in AIA 304 Å (blue curve), the reconnection flux during the flare (pink curve), the time derivative of the reconnection flux (gray curve), and the GOES flux. (b) The evolution of preflare ribbons in AIA 304 Å. (c) The preflare and flare ribbons in AIA 1600 Å. (d) The vertical current density maps before the eruption. Green contours mark the preflare and flare ribbons identified by bright pixels in AIA 304 Å and 1600 Å. An animation of the AIA 304 Å and AIA 1600 Å images is available. The animation proceeds from 00:00 UT on 2011 August 2 to 06:00 on 2011 August 2, showing preflare ribbons and flare ribbons.

(An animation of this figure is available in the online article.)

flux. The preflare ribbon flux reached the first peak at about 01:01 UT, when significant brightening occurred in the moving footpoint (FP−; Figure 6(b2)). About half an hour later, two smoothly bright ribbons appeared around the coronal coherent structure and started to expand outward (arrows in Figure 6(b3)) as the preflare ribbon flux reached its second peak. Then the preflare ribbon flux experienced two more rises in about 1 hr but hit bottom at about 03:40 UT. Less than 20 minutes later, the preflare ribbon flux rose steeply, suggesting the occurrence of a faster reconnection around the flux rope. From this moment, the preflare ribbons

were also observed in the AIA 1600 Å passband (Figures 6(c2) and (c3)). Subsequently, the preflare ribbons were rapid transformed into the flare ribbons (see the Figure 6 animation). The flare ribbons observed in the AIA 1600 Å passband enveloped the preflare ribbons and possessed a larger area, even encompassing portions of the footpoints of the eruptive MFR (FP+/− in Figure 6(c4)). Both the preflare ribbons observed in the AIA 304 Å passband and the flare ribbons observed in the AIA 1600 Å passband were found to be cospatial with significant nonneutralized currents (Figures 6(d1) and (d2)).
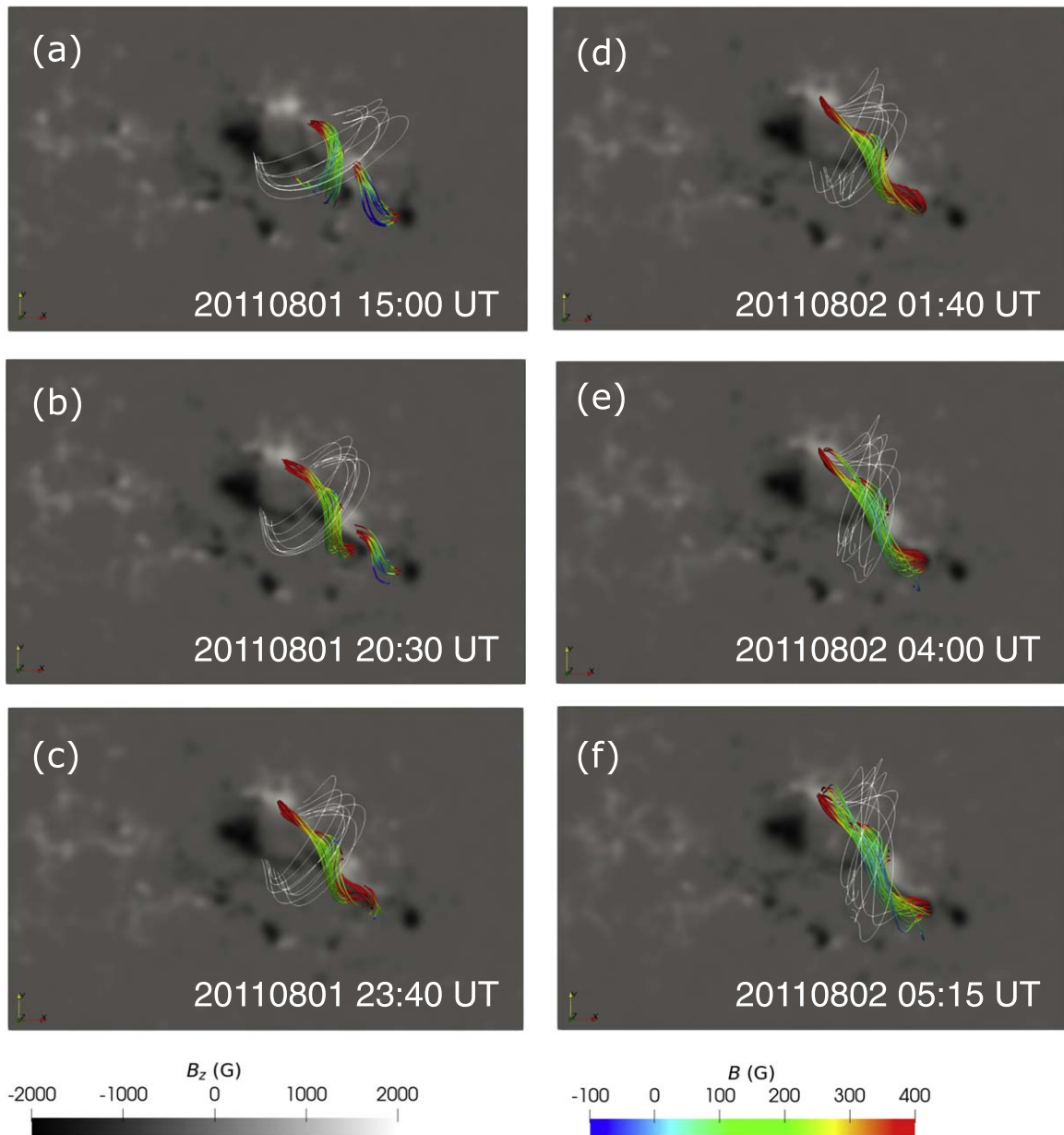
Figure 7. The simulation results for this event. Colorful lines show the simulated coronal structure. White lines show the overlying field.

6. Discussion

Here we present an unprecedented observation of the synchronous buildup of a preeruptive coherent structure in both the photosphere and the corona. A bright coherent structure was initially observed in the AIA 94 Å passband at August 1 19:30 UT, about 10 hr prior to the onset of the M-class flare. This coherent structure was eventually evolved into a twisted flux rope and erupted as a CME (Figure 1). During the preeruptive phase, the buildup of the MFR exhibited a strong correlation with the evolution of the photospheric field. The coherent structure appeared in the corona immediately following the simultaneous enhancement of the magnetic properties of the photospheric field (Figure 4). Impressively, the FP− of the coronal structure was moving along with the slow extension of the significant nonneutralized current in the photosphere simultaneously in the subsequent 5 hr. Multiple episodes of heating were found around the coronal

structure, resulting in the continuous temperature enhancement (Figure 3). Moreover, the peak temperature of the coronal structure coincided with the second peak of the magnetic properties of the photospheric field (Figure 4). Eventually, a twisted flux rope formed prior to the eruption, with its feet anchored in regions characterized by the strong magnetic field and electric current (Figure 2(a8)).

6.1. Slow Formation of a Coronal Flux Rope via Photospheric Evolution

The synchronous evolution between the preeruptive coronal structure and the photospheric field suggests that the formation of the coronal flux rope could be driven by slow photospheric evolution. In this event, strong shear flows were observed along the PIL region. The occurrence of strong shear flows in the host active region coincided impressively with the appearance of the coronal structure (Figure 5). The shear flows continued during

the preeruptive phase. These observations may remind us of previous models on MFR formation, like the tether-cutting reconnection model (R. L. Moore et al. 2001) and the zipper reconnection model (J. Threlfall et al. 2018), revealing the role of shear flows in facilitating the formation of the MFR via reconnection.

Further, we perform a full data-driven MHD simulation (Y. Guo et al. 2019) to model the formation process of the observed flux rope. We adopt a zero-β MHD modeling to simulate the dynamic evolution of this active region, wherein pressure and gravity in comparison to the Lorentz force are omitted in the low corona. The governing equations are as follows:

$$\frac{\partial \rho}{\partial t} + \nabla \cdot (\rho \boldsymbol{v}) = 0, \tag{1}$$

$$\frac{\partial (\rho \boldsymbol{v})}{\partial t} + \nabla \cdot (\rho \boldsymbol{v}\boldsymbol{v} - \boldsymbol{B}\boldsymbol{B}) + \nabla\left(\frac{\boldsymbol{B}^2}{2}\right) = 0, \tag{2}$$

$$\frac{\partial \boldsymbol{B}}{\partial t} + \nabla \cdot (\boldsymbol{v}\boldsymbol{B} - \boldsymbol{B}\boldsymbol{v}) = 0, \tag{3}$$

where ρ, $\boldsymbol{B}$, and $\boldsymbol{v}$ represent the density, magnetic field, and velocity, respectively. The MHD equations are solved using MPI-AMRVAC (C. Xia et al. 2018; R. Keppens et al. 2023). The computation domain is $[x_{\min}, x_{\max}] \times [y_{\min}, y_{\max}] \times [z_{\min}, z_{\max}] = [-117.3, 117.3] \times [-73.3, 73.3] \times [1, 147.6]$ Mm^3, with an effective mesh grid of $320 \times 200 \times 200$, using a two-level adaptive mesh refinement. Consequently, the highest resolution of this simulation is approximately $1''$. The initial magnetic fields are provided by NLFFF modeling, achieved by the magneto-frictional relaxation (Y. Guo et al. 2016), based on the vector magnetogram observed by SDO/HMI at August 1 14:12 UT, prior to the appearance of the elongated DC. In particular, since the original observed magnetic fields do not fully comply with the force-free assumption, we apply the method proposed by T. Wiegelmann et al. (2006) to remove the Lorentz force and torque. Regarding the atmosphere, we utilize a stratified hydrostatic solar atmosphere extending from the chromosphere to the solar corona (see J. H. Guo et al. 2024 for more details). To drive the dynamic evolution of the coronal magnetic fields, we implement a series of magnetic fields and the derived vector velocity fields in the photosphere from August 1 14:12 UT to August 2 05:24 UT, referred to as the $v - B$ driven boundary. The vector velocity fields are obtained using the DAVE4VM method. To enhance the stability of MHD simulation and ensure consistency with the initial NLFFF modeling, we also preprocess the input vector magnetograms using the technique of T. Wiegelmann et al. (2006). For more details on the implementation of the data-driven boundary condition, please refer to J. H. Guo et al. (2024).

Figure 7 illustrates the 3D magnetic field evolution from August 1 15:00 UT to August 2 05:15 UT, covering the entire preeruptive phase. In the beginning, the magnetic fields above the PIL are mainly represented by two groups of arcades (colorful lines in Figure 7(a)). At about 20:30 UT, one arcade evolved into a coherent shear arcade driven by shearing motions along the PIL. Subsequently, the shear arcade extended toward the other arcade and finally merged into a larger structure (Figure 7(d)). However, the twist number T_w (R. Liu et al. 2016) of the larger structure is less than 1. To
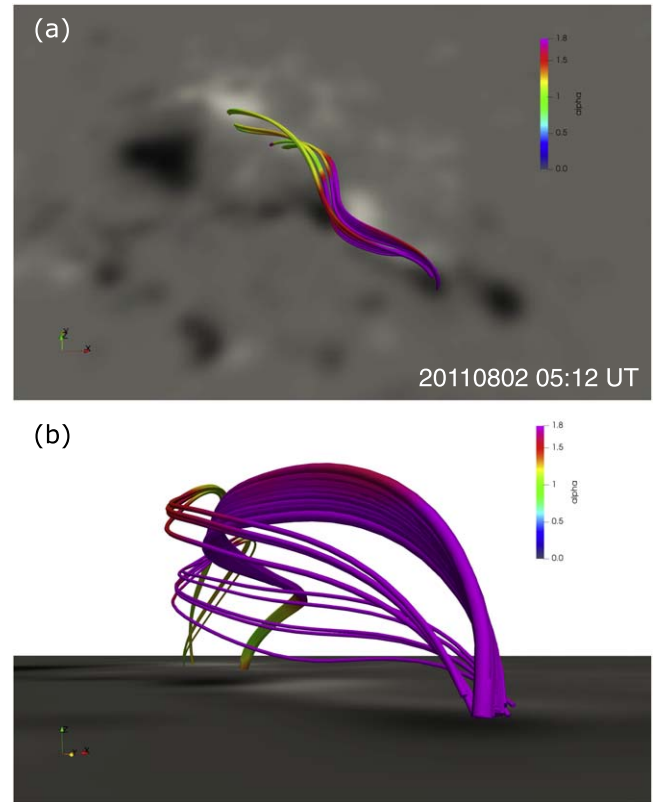

Figure 8. The force-free parameter α of the MFR at 05:12 UT on August 2. The field lines are color-coded by the value of $\alpha = J \cdot B/B^2$, which provides an estimate for the twist density of the magnetic field.

quantify the degree of twist in the flux rope, we visualize twisted field lines at August 2 05:12 UT (Figure 8), several minutes ahead of the onset of the flare. The field lines are color-coded by the value of the force-free parameter $\alpha = J \cdot B/B^2$, which provides an estimate for the twist density of the magnetic field. Many field lines exhibit significant twisting, with α values exceeding 2 (the maximum value reaching 4.33). These findings confirm that the preeruptive magnetic structure is indeed a flux rope. The large structure finally evolved into a highly twisted flux rope, i.e., with a twist number exceeding 1.0 (Figure 7(f)), and then erupted. The eruption in the simulation exhibits a slower rate than observations.

Previous studies have predicted that the emergence of a twisted flux tube would bring new currents into the photosphere, whose development is associated with the shearing flows (W. I. Manchester et al. 2004; V. Archontis & T. Török 2008). T. Török et al. (2014) conducted a subphotospheric twisted flux tube carrying neutralized current that emerged into the corona. During the emergence stage, the twisted flux tube brings significant nonneutralized current into the corona, forming the elongated DCs along the PIL region, exhibiting a similar evolution as the electric currents in our observations. We investigated the 3 days evolution of the host active region NOAA 11261 and found a significant flux emergence that commenced at July 31 14:00 UT and persisted for about 20 hr (Figure 9(b)). The host active region initially underwent decay until a new flux emergence occurred, characterized by the injection of opposite helicity fluxes (Figure 9(d)). The appearance of the nonneutralized current within the whole
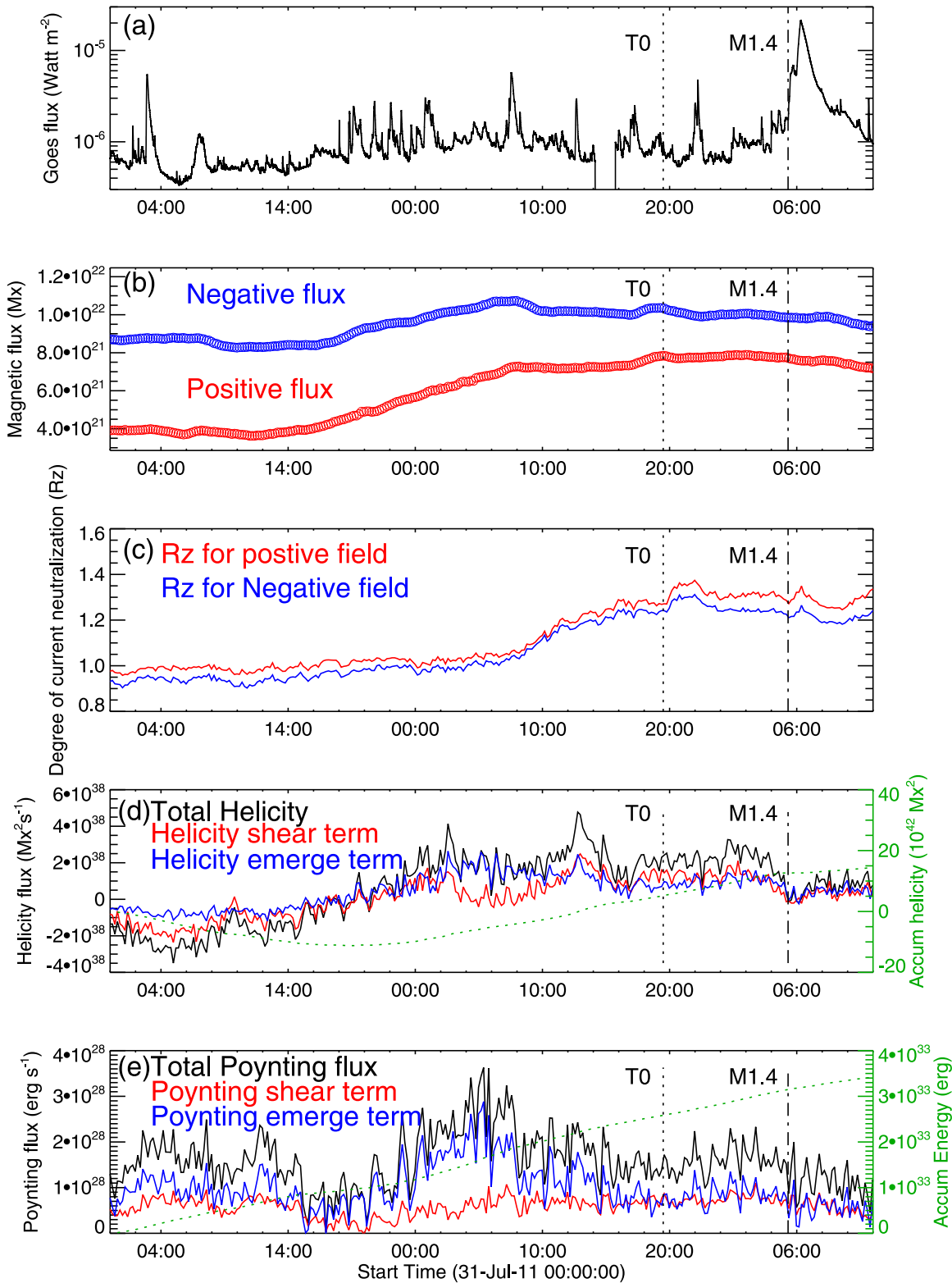
Figure 9. The temporal evolution of the host active region 11261 from July 31 00:00 UT to August 2 12:00 UT. (a) GOES soft X-ray flux. (b) The magnetic fluxes calculated in the active region (Figure 1(c)). (c) The degree of current neutralization |DC/RC|. (d) The relative helicity flux injection rate. (e) Poynting flux injection rate. Two vertical dashed lines mark the appearance of the coronal coherent structure in AIA 94 Å (T0) and the onset of the M1.4-class flare.

active region immediately followed the peak value of the helicity injection rate caused by the new flux emergence (Figure 9(c)). Furthermore, the nonneutralized current around the major PIL region became significant ($R_z > 2.0$) several hours ahead of the strong shearing flows (Figure 5(a)). Therefore, the coherent coronal structure observed at August 1 19:30 UT may be attributed to the emergence of a twisted flux tube.

6.2. Rapid Buildup of the Coronal Flux Rope by Preflare Intermittent Reconnection

The coronal coherent structure had experienced multiple episodes of heating since August 1 23:00 UT (Figure 3(c)), implying that magnetic reconnection occurred prior to the eruption. The preflare ribbon flux estimated from the AIA 304 Å observations exhibited multiple peaks, which were consistent with the peaks observed in the GOES soft X-ray flux (Figure 6(a)). Multiple peaks were also found in the mean temperature calculated at different components of the coherent structure (Figure 3). Moreover, the preflare ribbons were concentrated along the major PIL region with the significant nonneutralized current, manifested as a pair of current ribbons predicted as the 3D flare/CME model (M. Janvier et al. 2014). The aforementioned observations indicate the occurrence of intermittent reconnection beneath or wrapping around the flux rope.

Recently, a series of 3D numerical simulations suggested that an internal current sheet can be formed through quasi-static shear flows, ultimately triggering the reconnection and driving the eruption, regardless of the presence of a flux rope (C. Jiang et al. 2021; X. Bian et al. 2022, 2023; Q. Liu et al. 2024). In their models, the internal current sheet with high current density can form at a lower height, connecting to the photosphere. In our observations, the pair of current ribbons may highlight the footprints of the current sheet forming beneath the flux rope. Quantitative measurements of preflare reconnection fluxes revealed a 5 hr slow evolution followed by the rapid eruption (Figure 6). The 5 hr slow evolution may represent the gradual thinning of the current sheet until it reaches a critical thickness triggering fast reconnection. However, the duration of preflare reconnection in our observations exceeded 5 hr, significantly longer than in simulations or other observations.

6.3. Conclusion

In summary, we thoroughly investigated the complete evolution of a coronal flux rope with significant nonneutralized current from its formation to eruption. The flux rope originated from a coherent, low-lying bright structure, which could be attributed to the emergence of a twisted flux tube carrying significant DC. The coherent structure initially coevolved with the photospheric nonneutralized current and subsequently experienced intermittent reconnection in the corona, ultimately triggering the eruption. The remarkable synchronous evolution between the coronal coherent structure and the photospheric significant nonneutralized current may offer a new observational feature for detecting the preeruptive magnetic structure.

ORCID iDs

Wensi Wang ● https://orcid.org/0000-0002-9865-5245
Rui Liu ● https://orcid.org/0000-0003-4618-4979
Jiong Qiu ● https://orcid.org/0000-0002-2797-744X
Jinhan Guo ● https://orcid.org/0000-0002-4205-5566
Yuming Wang ● https://orcid.org/0000-0002-8887-3919

References

Antiochos, S. K., DeVore, C. R., & Klimchuk, J. A. 1999, ApJ, 510, 485
Archontis, V., & Hood, A. W. 2010, A&A, 514, A56
Archontis, V., & Hood, A. W. 2012, A&A, 537, A62
Archontis, V., Moreno-Insertis, F., Galsgaard, K., Hood, A., & O'Shea, E. 2004, A&A, 426, 1047
Archontis, V., & Török, T. 2008, A&A, 492, L35
Avallone, E. A., & Sun, X. 2020, ApJ, 893, 123
Awasthi, A. K., Liu, R., Wang, H., Wang, Y., & Shen, C. 2018, ApJ, 857, 124
Barczynski, K., Aulanier, G., Janvier, M., Schmieder, B., & Masson, S. 2020, ApJ, 895, 18
Bian, X., Jiang, C., Feng, X., Zuo, P., & Wang, Y. 2023, ApJ, 956, 73
Bian, X., Jiang, C., Feng, X., et al. 2022, A&A, 658, A174
Bobra, M. G., Sun, X., Hoeksema, J. T., et al. 2014, SoPh, 289, 3549
Cheng, X., Zhang, J., Ding, M. D., Liu, Y., & Poomvises, W. 2013, ApJ, 763, 43
Cheung, M. C. M., Boerner, P., Schrijver, C. J., et al. 2015, ApJ, 807, 143
Duan, A., Xing, Y., & Jiang, C. 2024, RAA, 24, 075005
Fan, Y. 2001, ApJL, 554, L111
Fan, Y., & Gibson, S. E. 2004, ApJ, 609, 1123
Georgoulis, M. K., Titov, V. S., & Mikić, Z. 2012, ApJ, 761, 61
Gibson, S. E., & Fan, Y. 2006, JGRA, 111, A12103
Gibson, S. E., Kucera, T. A., Rastawicki, D., et al. 2010, ApJ, 724, 1133
Guo, J. H., Ni, Y. W., Guo, Y., et al. 2024, ApJ, 961, 140
Gou, T., Liu, R., Veronig, A. M., et al. 2023, NatAs, 7, 815
Guo, Y., Xia, C., Keppens, R., Ding, M. D., & Chen, P. F. 2019, ApJL, 870, L21
Guo, Y., Xia, C., Keppens, R., & Valori, G. 2016, ApJ, 828, 82
Green, L. M., Kliem, B., Török, T., van Driel-Gesztelyi, L., & Attrill, G. D. R. 2007, SoPh, 246, 365
Green, L. M., Kliem, B., & Wallace, A. J. 2011, A&A, 526, A2
Hood, A. W., & Priest, E. R. 1979, SoPh, 64, 303
Janvier, M., Aulanier, G., Bommier, V., et al. 2014, ApJ, 788, 60
Jiang, C., Feng, X., Liu, R., et al. 2021, NatAs, 5, 1126
Kaiser, M. L., Kucera, T. A., Davila, J. M., et al. 2008, SSRv, 136, 5
Keppens, R., Popescu Braileanu, B., Zhou, Y., et al. 2023, A&A, 673, A66
Kliem, B., & Török, T. 2006, PhRvL, 96, 255002
Kliem, B., Török, T., Titov, V. S., et al. 2014, ApJ, 792, 107
Kontogiannis, I., & Georgoulis, M. K. 2024, ApJ, 970, 162
Kontogiannis, I., Georgoulis, M. K., Guerra, J. A., Park, S.-H., & Bloomfield, D. S. 2019, SoPh, 294, 130
Leake, J. E., Linton, M. G., & Török, T. 2013, ApJ, 778, 99
Leka, K. D., Canfield, R. C., McClymont, A. N., & van Driel-Gesztelyi, L. 1996, ApJ, 462, 547
Lemen, J. R., Title, A. M., Akin, D. J., et al. 2012, SoPh, 275, 17
Liu, Q., Jiang, C., Bian, X., et al. 2024, MNRAS, 529, 761
Liu, R., Kliem, B., Titov, V. S., et al. 2016, ApJ, 818, 148
Liu, R., Kliem, B., Török, T., et al. 2012, ApJ, 756, 59
Liu, R., Liu, C., Wang, S., Deng, N., & Wang, H. 2010, ApJL, 725, L84
Liu, R., & Wang, W. 2024, ApJ, 973, 50
Liu, Y., Sun, X., Török, T., Titov, V. S., & Leake, J. E. 2017, ApJL, 846, L6
Liu, Y., Török, T., Titov, V. S., et al. 2024, ApJ, 961, 148
Longcope, D. W., & Welsch, B. T. 2000, ApJ, 545, 1089
Magara, T., & Longcope, D. W. 2003, ApJ, 586, 630
Manchester, W. I., Gombosi, T., DeZeeuw, D., & Fan, Y. 2004, ApJ, 610, 588
Melrose, D. B. 1991, ApJ, 381, 306
Moore, R. L., & Roumeliotis, G. 1992, in IAU Colloq. 133: Eruptive Solar Flares, ed. Z. Svestka, B. V. Jackson, & M. E. Machado (New York: Springer), 69
Moore, R. L., Sterling, A. C., Hudson, H. S., & Lemen, J. R. 2001, ApJ, 552, 833
Parker, E. N. 1996, ApJ, 471, 485
Patsourakos, S., Vourlidas, A., Török, T., et al. 2020, SSRv, 216, 131
Pesnell, W. D., Thompson, B. J., & Chamberlin, P. C. 2012, SoPh, 275, 3
Qiu, J., & Cheng, J. 2017, ApJL, 838, L6
Qiu, J., Hu, Q., Howard, T. A., & Yurchyshyn, V. B. 2007, ApJ, 659, 758
Rust, D. M., & Kumar, A. 1996, ApJL, 464, L199

Savcheva, A. S., McKillop, S. C., McCauley, P. I., Hanson, E. M., & DeLuca, E. E. 2014, SoPh, 289, 3297

Schuck, P. W. 2008, ApJ, 683, 1134

Su, Y., Veronig, A. M., Hannah, I. G., et al. 2018, ApJL, 856, L17

Threlfall, J., Hood, A. W., & Priest, E. R. 2018, SoPh, 293, 98

Török, T., & Kliem, B. 2005, ApJL, 630, L97

Török, T., Leake, J. E., Titov, V. S., et al. 2014, ApJL, 782, L10

van Ballegooijen, A. A., & Martens, P. C. H. 1989, ApJ, 343, 971

Wang, W., Liu, R., Wang, Y., et al. 2017, NatCo, 8, 1330

Wang, W., Qiu, J., Liu, R., et al. 2023, ApJ, 943, 80

Wang, W., Zhu, C., Qiu, J., et al. 2019, ApJ, 871, 25

Webb, D. F., Cliver, E. W., Crooker, N. U., Cry, O. C. S., & Thompson, B. J. 2000, JGR, 105, 7491

Wiegelmann, T., Inhester, B., & Sakurai, T. 2006, SoPh, 233, 215

Xia, C., Teunissen, J., El Mellah, I., Chané, E., & Keppens, R. 2018, ApJS, 234, 30

Xing, C., Cheng, X., & Ding, M. D. 2020, Innov, 1, 100059

Zhang, J., Cheng, X., & Ding, M.-D. 2012, NatCo, 3, 747